# 1.4 Å Structure of Photoactive Yellow Protein, a Cytosolic Photoreceptor: Unusual Fold, Active Site, and Chromophore[†,‡]

Gloria E. O. Borgstahl, DeWight R. Williams, and Elizabeth D. Getzoff*

*Department of Molecular Biology, The Scripps Research Institute, La Jolla, California 92037*

*Received February 13, 1995; Revised Manuscript Received March 29, 1995*[⊗]

ABSTRACT: A photosensing protein directs light energy captured by its chromophore into a photocycle. The protein's structure must accommodate the photocycle and promote the resulting chemical or conformational changes that lead to signal transduction. The 1.4 Å crystallographic structure of photoactive yellow protein, determined by multiple isomorphous replacement methods, provides the first view at atomic resolution of a protein with a photocycle. The $\alpha/\beta$ fold, which differs from the original chain tracing, shows striking similarity to distinct parts of the signal transduction proteins profilin and the SH2 domain. In the dark state structure of photoactive yellow protein, the novel 4-hydroxycinnamyl chromophore, covalently attached to Cys69, is buried within the major hydrophobic core of the protein and is tethered at both ends by hydrogen bonds. In the active site, the yellow anionic form of the chromophore is stabilized by hydrogen bonds from the side chains of Tyr42 and buried Glu46 to the phenolic oxygen atom and by electrostatic complementarity with the positively charged guanidinium group of Arg52. Thr50 further interlocks Tyr42, Glu46, and Arg52 through a network of active site hydrogen bonds. Arg52, located in a concavity of the protein surface adjacent to the dominant patch of negative electrostatic potential, shields the chromophore from solvent and is positioned to form a gateway for the phototactic signal. Overall, the high-resolution structure of photoactive yellow protein supports a mechanism whereby electrostatic interactions create an active site poised for photon-induced rearrangements and efficient protein-mediated signal transduction.

How do bacteria and higher organisms transduce light via a protein photocycle? A complete understanding of this fundamental biological process requires atomic structural information, as well as detailed biochemical and biophysical studies, on a protein photoreceptor from an amenable biological system, such as a phototactic bacterium. The 1.4 Å crystal structure of photoactive yellow protein (PYP),[1] isolated from the extremely halophilic, purple, phototrophic bacterium *Ectothiorhodospira* halophila (Meyer, 1985), provides the first view at atomic resolution of a protein with a photocycle.

*E. halophila* live in sunny, hypersaline lakes (Imhoff et al., 1978) and exhibit a repellent response to blue light, presumably to select optimal light levels and living conditions. The action spectrum of the repellent response to blue light in *E. halophila* matches the absorption spectrum of PYP, implicating PYP as the photoreceptor for the negative phototactic response (Sprenger et al., 1993). PYP has also been purified from other phototrophic purple bacteria (Meyer et al., 1990, 1993) and identified immunologically in many other bacteria (Hoff et al., 1994b).

The PYP structure provides a basis for understanding other biologically important photoreceptors such as the retinal-containing rhodopsin family. These include the sensory rhodopsins (SRI and SRII), which mediate positive and negative phototaxis in the archaebacterium *Halobacterium halobium* by modulating a methylation/demethylation system which sends signals to the flagellar motor (Spudich et al., 1989; Spudich & Bogomolni, 1988); visual rhodopsin, which triggers the visual excitation cascade by binding the G protein transducin; and bacteriorhodopsin (bR) and halorhodopsin, the light-driven proton and chloride pumps. The structure of these seven-helix bundle proteins has been limited to much lower resolution by their transmembrane nature (Henderson et al., 1990; Schertler et al., 1993). Yet, comparisons of the existing bR structure (Henderson et al., 1990) to the refined 1.4 Å PYP structure may provide insights into common and distinct structural features allowing a protein photocycle.

The time course of PYP's reversible photocycle (Meyer et al., 1987) most closely resembles that of SRI (Bogomolni & Spudich, 1982), but PYP's distinctive bright yellow color originates from a 4-hydroxycinnamyl chromophore anion covalently linked to Cys69 by a thioester bond (Baca et al., 1994; Hoff et al., 1994a) rather than a Schiff-base-linked retinal. When a photon is absorbed by PYP, its dark state absorption maxima at 446 nm is red-shifted to 460 nm in $<10$ ns and then bleached ($k \sim 10^4$ s$^{-1}$) to 340 nm. The photocycle is completed by a slower return to the dark state ($k \sim 2$ s$^{-1}$) (Meyer et al., 1987; Ng et al., 1995). One proton is absorbed during formation of the fully bleached intermediate and released upon return to the dark state (Meyer et al., 1993). PYP's high efficiency [quantum yield of 0.64 as

[†] This work was supported by NIH Grant GM37684 to E.D.G. and NRSA Fellowship GM15820 to G.E.O.B.

[‡] PYP atomic coordinates (replacing the old $C_\alpha$ coordinates, Accession Number 1PHY) have been deposited in the Brookhaven Protein Data Bank, Accession Number 2PHY.

* Author to whom correspondence should be addressed.

[⊗] Abstract published in *Advance ACS Abstracts,* May 1, 1995.

[1] Abbreviations: PYP, photoactive yellow protein; SRI, sensory rhodopsin I; bR, bacteriorhodopsin; MIR, multiple isomorphous replacement; CAPS, 3-(cyclohexylamino)-1-propanesulfonic acid; PCMB, *p*-(chloromercuri)benzoate; SH2 domain, Src homology 2 domain.

0006-2960/95/0434-6278$09.00/0 

compared with 0.25 for bR (Meyer et al., 1989)], cytosolic location, water solubility, and temperature stability (Meyer et al., 1987) make it an attractive alternative for bR in optical data processing applications (Birge, 1990).

In the preliminary PYP structure report from this laboratory (McRee et al., 1989), the initial 2.4 Å resolution electron density map was misinterpreted as a $\beta$-clam fold. This was apparently due to unrecognized data problems (see Methods), coupled to the then unexpected power of X-PLOR refinement (Brünger et al., 1987) to produce low $R$-values even for incorrect folds (Jones et al., 1991). The chromophore identity was also unknown at that time. The originally reported $P6_3$ space group (McRee et al., 1986), the indexing of the heavy atom derivative data, the position and hand of each heavy atom, and the combination of the derivatives to produce the initial experimental electron density map (McRee et al., 1989) were all checked and found to be correct. However, repeated efforts to refine the $\beta$-clam fold failed, suggesting problems in the data and model, so the entire structure was redetermined from scratch using all new native and derivative data.

Herein, we report the determination and analysis of the 1.4 Å resolution PYP structure with the 4-hydroxycinnamyl chromophore. PYP's $\alpha/\beta$ fold shows surprising similarities with the eukaryotic signal transduction domains profilin and SH2, which may have evolutionary or functional significance. Thus, this PYP structural study, in conjunction with biochemical studies, may provide a more detailed and unified understanding of both protein photocycles and protein-mediated signal transduction. This first atomic structure for a protein with a photocycle suggests that electrostatic interactions may act to promote efficient signal transduction and to create an active site poised for photon-induced conformational change.

## METHODS

*Protein Purification.* PYP was purified (Baca et al., 1994) directly from *E. halophila* strain BN9626 (Meyer, 1985), as neither the molecular genetics techniques for the transformation of *E. halophila* nor the methodologies for overexpression of chromophore-containing protein in *Escherichia coli* have yet been developed.

*Crystallization.* Microseed solution was made by grinding large, grossly twinned crystals in 3.2 M $NH_4SO_4$ and 20 mM sodium phosphate, pH 7.0. Drops (10 $\mu$L) of protein solution (~15 mg/mL PYP in ~2.5 M $NH_4SO_4$ and 20 mM sodium phosphate, pH 7.0) on siliconized coverslips were injected with 0.5 $\mu$L of microseed solution, diluted (~500-fold) such that one to five crystals grew per drop, and suspended over 500-$\mu$L reservoirs of ~2.5 M $NH_4SO_4$ on Linbro plates. Crystals grew as long hexagonal rods (50−300 × >1000 $\mu$m) in space group $P6_3$ with unit cell dimensions $a$ = 66.9 Å, $b$ = 66.9 and $c$ = 40.8 Å (McRee et al., 1986).

*Native PYP Diffraction Data to 1.4 Å Resolution.* Native diffraction data were collected wtih Cu Kα radiation from a Rigaku RU-200 X-ray generator with a graphite monochromator by using a Siemens area detector and were processed with Xengen software (Howard et al., 1987). High-resolution native data (see Table 1) were collected on a single crystal (~250 × 250 × 500 $\mu$m) by using separate low- ($2\theta$ = 15°; data to 2.4 Å) and high-resolution runs ($2\theta$ = 50°; data to 1.3 Å). The native data were put on an absolute scale using SQUASH (Zhang & Main, 1990; Zhang, 1993).

*Problems with Previous $\beta$-Clam Fold.* Atomic models built from the previous $\beta$-clam chain trace and refined with original diffraction data (McRee et al., 1989) did not refine properly with the newly collected 1.4 Å resolution diffraction data set. Positional refinement with X-PLOR (Brünger et al., 1987) reduced the overall $R$-value from 50% to 37% for 10−2.5 Å resolution data, but the resulting omit maps were not interpretable. Unfavorable $\phi$, $\psi$ angles for 31% of the residues and inconsistency with the 19% helical content indicated by circular dichroism (Meyer et al., 1987) also suggested that the $\beta$-clam model was not correct. Therefore, the structure of PYP was completely redetermined using multiple isomorphous replacement (MIR) methods as outlined below.

Where possible, sources of error leading to the $\beta$-clam fold were checked. Problems were found with both the diffraction data and the model. Unrecognized errors in the bias setting on the Xentronics area detector and possibly crystal twinning apparently affected the original diffraction measurements, as old data would not merge properly with the new data used in this study ($R_{merge}$ ~20%). Standard MIR statistics were misleadingly good (McRee et al., 1989), causing the quality of the original MIR electron density map to be overestimated. Model errors apparently resulted from the above noted data problems coupled to the premature introduction of model bias into electron density maps, exclusion of low-resolution data (>5 Å) at early stages of refinement, and excessive simulated annealing refinement using X-PLOR, before its ability to reduce $R$-values despite errors was recognized (Jones et al., 1991). Map and model coordinate transformations associated with changes in both computer hardware and software have hampered our efforts to define the exact relationship between the $\beta$-clam fold and the new, correct $\alpha/\beta$ structure, making detailed comparisons impracticable.

*Heavy Atom Derivatives.* The original heavy atom derivatives (McRee et al., 1989) were reproduced and further optimized, and new heavy atom derivatives were found. Crystals were soaked overnight or for 7 h [$K_2PtCl_4$ derivative only (McRee et al., 1989)] in heavy atom solutions with 75−80% $NH_4SO_4$ or saturated $Na_2SO_4$ (Os derivative only) and with 20 mM buffer (Hepes, pH 7.0, citrate, pH 8.5, or CAPS, pH 10). New diffraction data were collected for all derivatives (see Table 1). Most heavy atom derivative diffraction data were collected with Cu Kα radiation from a Rigaku RU-200 X-ray generator with a graphite monochromator by using a Siemens area detector and were processed with Xengen software (Howard et al., 1987). Anomalous diffraction data for $GdSO_4$ and $K_2PtCl_4$ derivatives were collected from an Elliot GX-21 X-ray generator with focusing mirrors by using a Mar Research image plate detector and were processed with MOSFLM software (Leslie et al., 1986).

*MIR Phase Calculation.* XtalView software (McRee, 1992) was used to identify heavy atom positions in difference Patterson and cross-phased difference Fourier maps. Xheavy software (McRee, 1993) was used to refine parameters and calculate MIR phases (see Table 2). Anomalous diffraction data from $GdSO_4$ and $K_2PtCl_4$ derivatives confirmed the hand. After systematic evaluation of MIR map quality with and without each heavy atom derivative, the $K_2HgI_4$ derivative was excluded. All major heavy atom binding sites were distinct, except the common site for the lanthanides $GdSO_4$ and $Er(CH_3COO)_3$ (see Table 2).

Table 1: PYP Diffraction Data

| data set | resolution (Å) | completeness (%) | unique reflections (no.) | redundancy | $R_{sym}$[a] (%) | $R_{merge}$[b] |
|---|---|---|---|---|---|---|
| native | 1.4 | 91 | 18681 | 3.3 | 4.0 | |
| 10 mM $K_2Pt(CN)_4$, pH 7 | 2.2 | 95 | 4451 | 4.1 | 5.7 | 24.3 |
| satd PCMB, pH 10 | 2.2 | 99 | 4912 | 3.4 | 9.3 | 20.3 |
| 10 mM $KAu(CN)_2$, pH 7 | 2.2 | 95 | 4648 | 4.1 | 6.9 | 25.3 |
| 10 mM $KOsCl_6$, pH 8.5 | 2.8 | 88 | 2199 | 1.9 | 4.8 | 20.5 |
| 50 mM $Er(CH_3COO)_3$, pH 7 | 2.8 | 96 | 2747 | 4.4 | 4.0 | 9.8 |
| 50 mM $GdSO_4$, pH 7 | 2.8 | 91 | 2608 | 6.3 | 8.4 | 8.8 |
| 0.1 mM $K_2PtCl_4$, pH 7 | 2.8 | 91 | 2630 | 9.0 | 8.4 | 8.3 |

[a] $R_{sym}$ is the unweighted *R*-factor on intensities for multiple observations of symmetry-related reflections. [b] $R_{merge}$ is the unweighted *R*-factor on structure factor amplitudes for all reflections in common with the native data.

*Model Building, Crystallographic Refinement, and $R_{free}$ Calculation.* The molecular graphics program Xfit (McRee, 1992) was used for electron density map calculation, display, and fitting. The atomic model was refined with X-PLOR (Brünger et al., 1987, 1990). $F_o - F_c$ omit electron density maps were made by systematically omitting 10% of the atoms from the model and refining the protein coordinates by simulated annealing before calculating structure factor amplitudes and phases.

The free *R*-value ($R_{free}$) (Brünger, 1992, 1993) was calculated as a final check of the quality of the crystallographic structure (see Table 3). Water molecules and dual conformers were deleted from the final refined structure, and this truncated model was refined against 90% of the diffraction data (20−1.4 Å resolution) with simulated annealing refinement, followed by temperature factor (*B*-value) refinement. Then water molecules and dual conformers were added back, and this whole model was refined against 90% of the data by conventional refinement, followed by *B*-value refinement. Then the $R_{free}$ was calculated with the remaining 10% of the data (not used in previous refinement).

*Surface and Electrostatic Calculations.* For the surface and electrostatic calculations, polar hydrogen atoms were added with X-PLOR (Brünger et al., 1987). Partial charges were assigned to atoms with AMBER (Weiner et al., 1984). The calculated net charge on PYP is −6 at pH 7, corresponding to the experimental p*I* of 4.3 (McRee et al., 1986). The net charge on the hydrogen-bonded Glu46−chromophore pair was −1. The Coulombic electrostatic potential was calculated 1.4 Å from the molecular surface (at the center of a water-sized probe) with the program ESPOT (Roberts et al., 1991) by using a distance-dependent dielectric constant of 5*r*, where *r* is the distance between an assigned partial charge at an atom center and the calculation point. This allowed the dielectric constant to reach 80 (dielectric constant for water) at about five water layers (5 × 3.2 = 16 Å) from the protein surface. The calculated electrostatic potentials were then color-mapped onto the molecular surface: red = −13 to −4, yellow = −4 to −2, green = −2 to 2, blue = 2 to 9 kcal/mol. Solvent-accessible molecular surface areas were calculated with MS software (Connolly, 1983) using a 1.4 Å radius probe.

## RESULTS AND DISCUSSION

*Structure Determination.* The 1.4 Å resolution structure of PYP in the dark state was determined by multiple isomorphous replacement (MIR) using seven heavy atom derivatives (Table 1). The MIR electron density map was readily interpretable (Figure 1A), with figures of merit of 0.89 for all reflections to 2.8 Å resolution and 0.75 for all data to 2.2 Å resolution (Table 2). This independent structure determination, using new diffraction data for native and both new and original heavy atom derivatives, showed that the original β-clam $C_\alpha$ trace (McRee et al., 1989) was not correct (see Methods).

This new structure determination was successful because we improved the protein purification (Meyer, 1985) and crystallization methods (McRee et al., 1986) to eliminate twinning, making large single crystals reproducibly available (Baca et al., 1994). This made an extensive heavy atom derivative search possible and led to the development of new and better heavy atom derivatives [Tables 1 and 2; $K_2Pt(CN)_4$, PCMB, $KAu(CN)_2$, and $KOsCl_6$], including some resulting from exotic soak conditions such as pH 10. Although the original heavy atom derivatives (McRee et al., 1989) [Tables 1 and 2; $Er(CH_3COO)_3$, $GdSO_4$, and $K_2PtCl_4$] were optimized, new heavy atom derivatives provided more phasing information (evident in larger values for $R_{merge}$ and phasing power), gave better estimates of closure error, and showed that the original derivatives had much lower phasing power than previously calculated.

A completely new atomic model was built into the 2.2 Å resolution MIR map from the C- to N-terminus. This map (Figure 1A) had no breaks in main-chain connectivity, all but seven carbonyl oxygen atoms could be well placed, and the amino acid sequence (Baca et al., 1994) could be properly registered for all residues except Met1. This initial atomic model was refined with conventional crystallographic refinement (Brünger et al., 1987), first with diffraction data from 20.0 to 3.0 Å resolution and then extending the resolution to 2.0 Å. Simulated annealing and temperature factor (*B*-value) refinement (Brünger et al., 1990) reduced the *R*-value to 26.5% with all main-chain dihedral angles ($\phi$, $\psi$ pairs) in normally allowed regions on the Ramachandran plot. Further cycles of omit electron density map fitting and crystallographic refinement included placing Met1, refitting the N-terminal pentapeptide, extending the resolution to 1.4 Å, modeling discretely disordered residues 4, 10, 33, 74, 87, 89, 116, and 124 with dual conformations, and adding 92 ordered water molecules and the chromophore to the model.

The 1.4 Å resolution electron density omit map identified the chromophore as a single, planar, six-membered ring with one substituent located para to the branched four-atom link to $S_\gamma$ Cys69 and when color-coded by the gradient of the electron density actually distinguished individual atom types within the chromophore (Figure 1B). The identity of the chromophore, a 4-hydroxycinnamyl anion, and its thioester linkage to Cys69 was confirmed by chemical cleavage studies and high-resolution mass spectrometry (Baca et al., 1994).

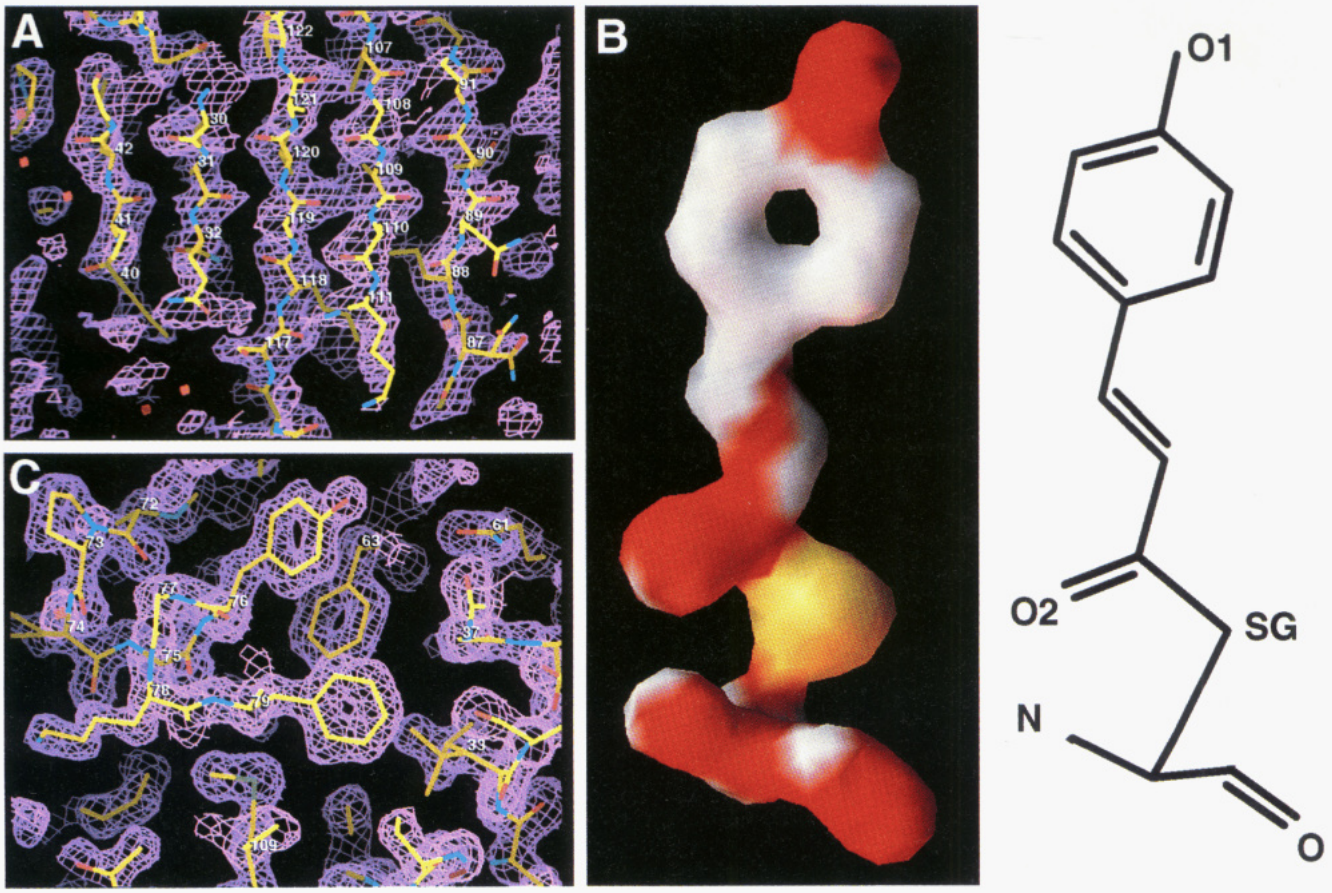


FIGURE 1: Refined, dark-state structure of PYP and electron density maps. (A) The 2.2 Å resolution experimental MIR map contoured at 1$\sigma$ for five $\beta$-strands (shown vertically). The high quality of the experimental map is demonstrated by the carbonyl oxygen bulges in the electron density, clearly showing the direction of the chain trace. The model is colored with carbon in yellow, oxygen in red, nitrogen in blue, and sulfur in green. (B) The electron density map and matching schematic diagram for the chromophore. Shown is the 1.4 Å resolution omit $F_o - F_c$ electron density map of the 4-hydroxycinnamyl chromophore, where the coordinates of the chromophore were omitted and the protein coordinates refined by simulated annealing before the phase calculation for the map. The electron density map is contoured at 4$\sigma$ and colored by the gradient (Purvis & Culberson, 1986) of the electron density: yellow > red > white. In this view, the Cys69 main chain (red and white) runs from left to right at the bottom, and the Cys69 side chain protrudes back and then up to SG (yellow), through the thioester linkage (red, left center, O2), and double bond (red and white, center), to the phenolic ring (white, top). For the chromophore side chain, the sulfur atom SG (yellow), phenolic oxygen O1, and thioester oxygen O2 (both red) are distinguishable from the carbon atoms (white) by the steeper gradient and higher values of their electron density, as is the double bond between the phenolic ring and thioester linkage. In the dark state of PYP, the negative charge on the chromophore is delocalized on the ring, and the bond to the phenolic oxygen O1 has significant double bond character (Baca et al., 1994). The thioester oxygen (O2) is 23° out of the plane formed by the aromatic ring and linking double bond. (C) The 1.4 Å resolution $2F_o - F_c$ electron density map contoured at 1$\sigma$ near the major hydrophobic core. The model is colored as in part A. For parts A and C, images were made using XtalView (McRee, 1992), and for part B, the image was rendered with the program AVS (Upson et al., 1989).

The accuracy of the PYP structure is further indicated by the obvious holes in the electron density of amino acids with six-membered (and even five-membered) rings (Figure 1C).

The final refined PYP model has an overall conventional $R$-value of 18.6% for 16 794 reflections, including data between 20 and 1.4 Å resolution with a signal-to-noise ratio ($I/\sigma I$) greater than 3 (Table 3). These diffraction data are 88% complete from 20 to 1.5 Å resolution and 53% complete for the highest (1.5−1.4 Å) resolution data (Table 3). The overall $R_{free}$ for the PYP model without dual conformers and water molecules (26.8%) decreased to 22.6% when they were added back (see Methods). This $R_{free}$ is at the low end of the range reported for refined structures (Brünger & Nilges, 1993). The $R_{free}$ is fairly level for data between 8 and 1.4 Å resolution ($R_{free}$ for the 8−2.4 Å shell is 20.4%). The lack of a solvent continuum model elevates the $R_{free}$ at low resolution (20−8 Å) to 45.6%, resulting in a slightly elevated $R_{free}$ of 23.2% in the lowest resolution (20−2.4 Å) shell given in Table 3.

The refined PYP atomic coordinates have excellent stereochemistry. Root mean square deviations from ideality of bond lengths and angles are 0.012 Å and 1.57°, respectively (Table 3). The final model has no outliers on the Ramachandran plot and only 10 non-glycine residues (9.4%) outside the most energetically favored regions (Figure 2A). PYP has fairly low isotropic atomic $B$-values (Figure 2B) with an overall average $B$-value of 13.2 Å$^2$: 11.6 Å$^2$ for protein atoms and 29.4 Å$^2$ for waters. $B$-values for water molecules range from 9.0 to 52.8 Å$^2$ with a standard deviation of 11.6 Å$^2$.

*Overall Protein Fold.* PYP has an $\alpha/\beta$ fold (Figure 2C) characterized by a central, twisted, 6-stranded, antiparallel $\beta$-sheet flanked on both sides by loops and helices (Figure 3). On one side of the $\beta$-sheet, the N-terminal 28 residues form a lariat-like loop structure (termed the helical lariat), including helices $\alpha$1 and $\alpha$2, that is closed by main-chain hydrogen bonds from residues 2 and 4 to residues 25 and 27. Next, a $\beta$-hairpin ($\beta$1 and $\beta$2 linked by a type I turn)

Table 2: Refined Heavy Atom Derivative Parameters of PYP Derivatives

| derivative | site no. | occupancy[a] | $x$[b] | $y$ | $z$ | $R_{Cullis}$ (%) ($R_{culanom}$)[c] | phasing power[d] | protein neighbors[e] |
|---|---|---|---|---|---|---|---|---|
| 10 mM $K_2Pt(CN)_4$, pH 7 | 1 | 1.00 | 0.046 | 0.322 | 0.357 | 50.7 | 1.90 | Arg52#0, Val57#0, Lys60#0, Val66#0, |
| | | | 19.872 | −2.752 | −26.234 | | | Glu74#4, Lys78#4 |
| satd PCMB, pH 10 | 1 | 1.00 | 0.045 | 0.180 | 0.214 | 48.6 | 1.75 | Gln99#0, Glu74#4, Tyr94#4 |
| | | | 10.527 | −2.520 | −32.069 | | | |
| 10 mM $KAu(CN)_2$, pH 7 | 1 | 1.00 | 0.248 | 0.013 | 0.045 | 63.7 | 1.66 | Phe6#0, Gly7#0, Met91#0, Lys106#0, |
| | | | 16.099 | 0.736 | 1.836 | | | Ser72#4, Pro73#4 |
| | 2 | 0.43 | 0.053 | 0.317 | 0.362 | | | Arg52#0, Gln56#0, Val57#0, Lys60#0, |
| | | | 19.508 | −3.535 | −25.993 | | | Glu74#4, Lys78#4 |
| 10 mM $KOsCl_6$, pH 8.5 | 1 | 1.00 | 0.006 | 0.283 | 0.295 | 66.2 | 1.54 | Lys60#0, Glu74#4, Lys78#4 |
| | | | 18.979 | −0.637 | −28.767 | | | |
| | 2 | 0.65 | 0.040 | 0.396 | 0.172 | | | Ser8#0, Pro73#4, Glu81#4 |
| | | | 24.709 | −2.288 | 7.210 | | | |
| | 3 | 0.90 | 0.138 | 0.544 | 0.088 | | | His3#0, Lys17#0, Asp34#3, Asp116#3 |
| | | | 31.654 | −8.210 | 3.435 | | | |
| 50 mM $Er(CH_3COO)_3$, pH 7 | 1 | 1.00 | 0.499 | 0.105 | 0.120 | 61.3 | 1.43 | Glu9#0, Asp10#0, Asp19#3, Asp20#3 |
| | | | 29.878 | 6.095 | 4.896 | | | |
| 50 mM $GdSO_4$, pH 7 | 1 | 1.00 | 0.502 | 0.107 | 0.120 | 62.7 (42; 3.5 Å) | 1.31 | Glu9#0, Asp10#0, Asp19#3, Asp20#3 |
| | | | 30.055 | 6.205 | 4.896 | | | |
| 0.1 mM $K_2PtCl_4$, pH 7 | 1 | 1.00 | 0.261 | 0.068 | 0.000 | 63.0 (48; 5.0 Å) | 1.28 | Met91#0, Lys106#0, Gly51#5 |
| | | | 15.216 | 3.946 | 0.000 | | | |

[a] Occupancy of the major site was fixed at 1.0 and minor sites were refined; the $B$-value was fixed at 20.0 Å$^2$ for all sites. [b] $x$, $y$, $z$ coordinates in the fractional unit cell (first line) and orthogonal (in Å) (second line) in the reference frame of the protein model. [c] $R_{Cullis} = \sum[|F_h| - (|F_{ph}| - |F_p|)]/\sum|F_h|$; $R_{culanom}$ was calculated for the top 25% largest Bijvoet differences, with anomalous resolution cutoff indicated separately. [d] Phasing power is the ratio of the rms calculated heavy atom structure factor amplitudes to the rms lack of closure. [e] Includes all side chains within 5 Å; side chains within 4 Å are underlined; the molecule number in the crystal lattice is given, parent molecule labeled #0 (coordinates $x$, $y$, $z$) and symmetry-related molecules labeled #3 ($-x$, $-y$, $^1/_2 + z$), #4 ($y$, $y - x$, $^1/_2 + z$), and #5 ($x - y$, $x$, $^1/_2 + z$).

Table 3: PYP Native Data and Refinement Statistics

| | | | | | |
|---|---|---|---|---|---|
| data collection | | | | | |
| resolution (Å, by shell) | ∞−2.4 | 2.4−1.9 | 1.9−1.6 | 1.6−1.5 | 1.5−1.4 |
| no. of observations | 37597 | 7369 | 6335 | 5694 | 4910 |
| no. of unique reflections | 4319 | 4197 | 4003 | 3788 | 3449 |
| no. of unique reflections missing | 6 | 76 | 236 | 451 | 776 |
| average $I/\sigma(I)$[a] | 13.8 | 18.9 | 5.1 | 3.0 | 1.7 |
| $R_{sym}$ (%)[b] | 4.3 | 3.9 | 7.5 | 12.8 | 20.7 |
| refinement | | | | | |
| no. of non-hydrogen protein atoms[c] | 1022 | | | | |
| no. of water molecules | 92 | | | | |
| rms deviation, bond length (Å) | 0.012 | | | | |
| rms deviation, bond angle (deg) | 1.57 | | | | |
| resolution (Å, by shell) | 20−2.4 | 2.4−1.9 | 1.9−1.6 | 1.6−1.5 | 1.5−1.4 |
| no. of reflections ($F > 3\sigma$) | 4097 | 3993 | 4624 | 2050 | 2030 |
| completeness (%) | 98.4 | 95.7 | 83.7 | 69.5 | 53.2 |
| $R$-factor (%)[d] | 17.2 | 17.5 | 19.4 | 20.5 | 21.2 |
| $R_{free}$ (%) | 23.2 | 20.5 | 21.1 | 20.4 | 22.2 |
| resolution (Å, cumulative) | 20−2.4 | 20−1.9 | 20−1.6 | 20−1.5 | 20−1.4 |
| no. of reflections ($F > 3\sigma$) | 4097 | 8090 | 12714 | 14764 | 16794 |
| completeness (%) | 98.4 | 97.0 | 91.7 | 87.8 | 81.4 |
| $R$-factor (%) | 17.2 | 17.3 | 17.9 | 18.2 | 18.6 |
| $R_{free}$ (%) | 23.2 | 22.3 | 22.2 | 22.4 | 22.6 |

[a] $I$ is the observed intensity and $\sigma(I)$ is the standard deviation of $I$. [b] $R_{sym}$ is $\sum(|I_i - I_{av}|/I_{av})/n$ for all $n$ observations of symmetry-related reflections. [c] Including 987 atoms in the main conformation and 35 atoms in dual conformers. [d] $R$-factor = $\sum||F_o| - |F_c||/\sum|F_o|$, where $|F_o|$ and $|F_c|$ are observed and calculated structure factor amplitudes, respectively.

begins the β-sheet from the middle. Helices α3 and α4, short strand β3, the chromophore loop, and helix α5 span across the other side of the β-sheet to form the active site. The chromophore loop (residues 63−74) begins with one turn of π-helix ($n + 5$ hydrogen bonds) and ends with three type I turns (Figure 2C). C-Terminal residues 88−125 form the final three β-strands. The three strands in each half of the β-sheet (N-terminal β1, β2, β3 and C-terminal β4, β5, β6) have nearest neighbor connectivity. The β-sheet has unusual topology with the terminal strands (β1 and β6) in the middle and strands β3 and β4 on the outside.

PYP has two hydrophobic cores, one on each side of the central β-sheet. In the major core, the 4-hydroxycinnamyl chromophore and residues from the chromophore loop (Phe63, Val66, and Ala67) face four residues from the three N-terminal β-strands (Ile31, Leu33, Ile39, and Phe62), three residues from each of the three C-terminal β-strands (Leu88, Phe92, Phe96, Val105, Val107, Met109, Tyr118, Val120, and Val122), and four residues from the flanking α-helices (Val57, Phe75, and Phe79) and loop (Tyr42). Interestingly, the major core has two small holes (or "packing defects") on either side of Val120, each approximately the size of a water molecule, although empty. In the minor core, seven residues from the helical lariat (Phe6, Ile11, Leu15, Met18, Leu23, Leu26, and Phe28) interact with three residues from the middle β-strands β1 and β6 (Ala30, Trp119, and Phe121).

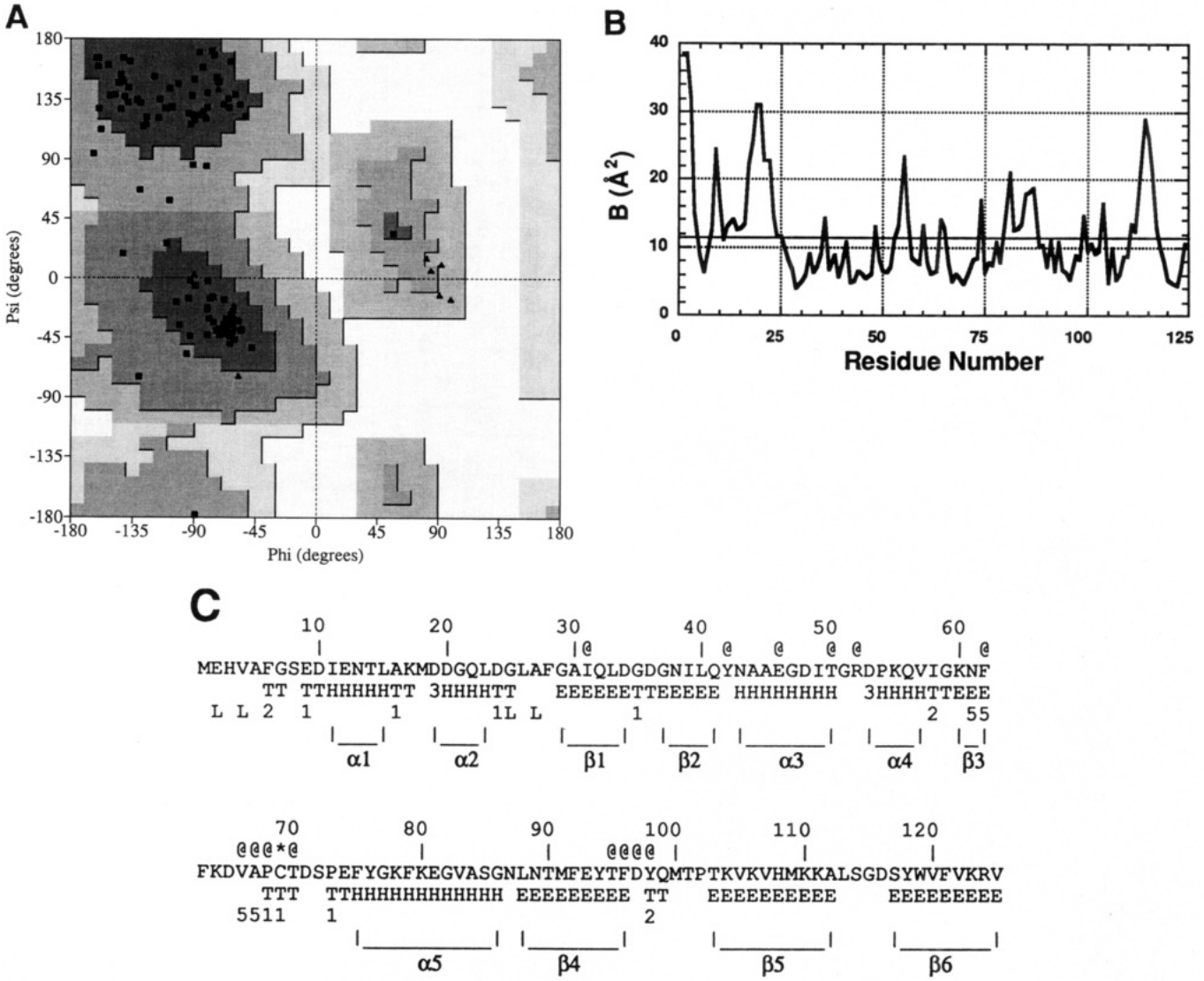


FIGURE 2: Conformation and crystallographic temperature factors of PYP. (A) Ramachandran diagram (Ramachandran & Sasisekharan, 1968) of the $\phi$, $\psi$ main-chain dihedral angles for PYP. Gly residues are indicated by filled triangles and non-glycine residues by filled squares. The most energetically favored regions are shaded dark gray. The high quality of PYP's stereochemistry was verified with PROCHECK (Laskowski et al., 1993). (B) Average crystallographic temperature factors ($B$-value) per residue of PYP. The average $B$-value for the protein (11.6 Å$^2$) is indicated with a solid horizontal line. (C) Secondary structure assignment of PYP's 125 residues. The amino acid sequence numbers are on line 1. On line 2, @ marks the residues within 4 Å of the chromophore, and the star indicates the cysteine residue where the chromophore is attached. Line 3 indicates the sequence of PYP in one-letter code (Baca et al., 1994). Residue assignments to secondary structural elements based on hydrogen bonding (Kabsch & Sander, 1983) are coded on line 4: H, α-helix ($n$ + 4 main-chain hydrogen bonding); 3, $3_{10}$ helix ($n$ + 3 main-chain hydrogen bonding); E, $\beta$-strand; T, residues 2 and 3 of a tight turn. On line 5, the second residue of type I (indicated by a 1) and type II tight turns (indicated by a 2), the residues closing the helical lariat (L), and the residues forming the $n$ + 5 main-chain hydrogen bonds for one turn of $\pi$-helix (indicated by a 5) are labeled. Lines 6 and 7 show the boundaries of the helices (α1 through α5) and $\beta$-strands ($\beta$1 through $\beta$6). In PYP, 28% of the residues are α-helix and 34% are $\beta$-sheet, which is in good agreement with UV circular dichroism measurements (Meyer et al., 1987).

*Comparison to Other Protein Folds.* The PYP fold shares distinct, but overlapping, structural and topological motifs (Figure 4) with regulatory proteins profilin (Schutt et al., 1993) and the Src homology 2 (SH2) domain (Waksman et al., 1992), although no sequence homology is apparent. Such structural similarities are of interest, as they can reveal evolutionary or functional relationships (Holm & Sander, 1990). Perhaps these structural motifs are common among proteins involved in signal transduction cascades, with different signal transduction functionalities decorating a structurally stable core of the appropriate size and shape.

Profilin binds actin (Tilney et al., 1983) and appears to link receptor-mediated transmembrane signaling to microfilament-based motility, through the second messenger phosphatidylinositol 4,5-bisphosphate (Lassing & Lindberg, 1985). Profilin and PYP share five antiparallel $\beta$-strands of unusual topology, identical sequence connectivity, and twist (Figure 4). Both proteins share a N-terminal helical loop (cyan, Figure 4), and both have two hydrophobic cores in identical locations. Differences in conformation are limited to the termini and the central sequence spanning the $\beta$-sheet, which also differ in function between the two proteins.

SH2 domains bind phosphotyrosine and communicate the phosphorylation state of key proteins to the signal transduction pathway (Koch et al., 1991). The SH2 domain matches the sequence connectivity, α-helix (green), loop conformation, and $\beta$-sheet topology and twist (Figure 4) of the C-terminal half of PYP. The active sites of PYP (anionic, tyrosine-like chromophore) and SH2 (bound phosphotyrosine peptide) are in a similar spatial location relative to the three

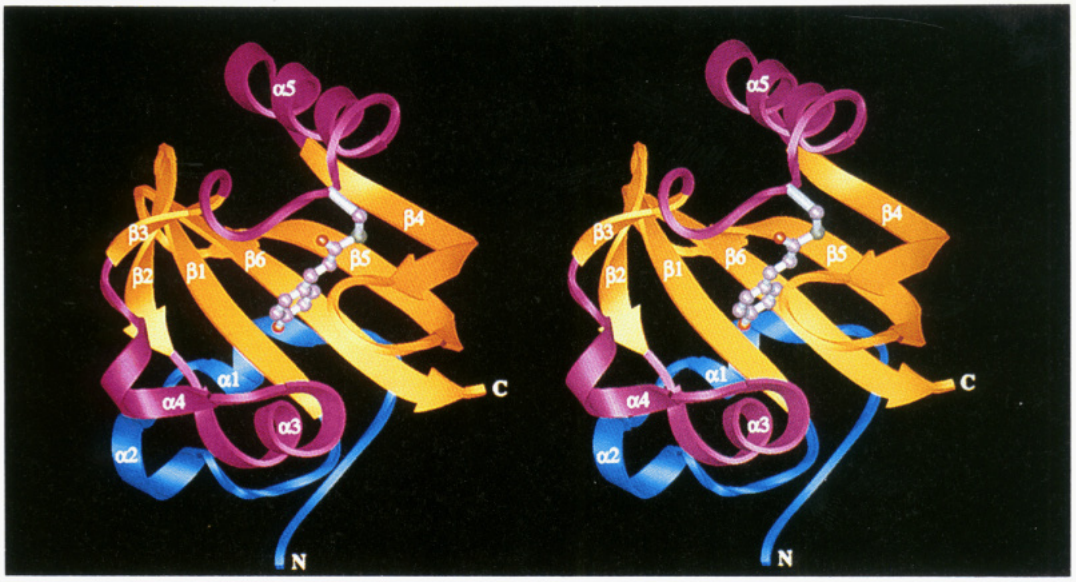


FIGURE 3: Stereoview of the PYP fold. The 125-residue polypeptide chain trace is shown as a RIBBONS drawing (Carson, 1991). The 4-hydroxycinnamyl chromophore position is represented with balls and sticks (lavender carbons, red oxygens, and a green sulfur). The helical lariat (including the N-terminus and α-helices α1 and α2) is in blue, the central β-sheet (including strands β1 through β6) is in yellow, and α-helices (α3, α4, and α5) and the chromophore loop are in pink. In this view, PYP is about 35 Å high, 28 Å wide, and 35 Å deep.

common β-strands and α-helix, as has been frequently found among catalytically diverse enzymes with common structural motifs (Alexandrov & Gō, 1994). In effect, the structure of bacterial PYP is not only similar to the eukaryotic signal transduction domains, profilin and SH2, but also provides a common structural link between them.

*Active Site of the PYP Dark State*. Within the environment of folded PYP (Figure 5A), the 4-hydroxycinnamyl chromophore is covalently bound to Cys69 by a thioester linkage (Figure 1B) and tethered to the protein by a network of hydrogen bonds. Analysis of pH titrations and UV−visible spectroscopy of the protein-bound and chemically released chromophore showed that the 4-hydroxycinnamyl chromophore is negatively charged in the dark state (Baca et al., 1994). Careful crystallographic refinement of the bond length between the phenolic oxygen O1 and the aromatic ring of the chromophore with 1.4 Å diffraction data indicated a predominantly double bond (Baca et al., 1994). Resonance forms, for the chromophore with this double bond, delocalize the negative charge over the aromatic ring. The aromatic ring, conjugated double bond, and thioester linkage are completely buried in the major hydrophobic core, while the main chain and $C_\beta$ atom of Cys69 expose 37 Å$^2$ to solvent. The positively charged guanidinium group of Arg52 packs obliquely against the aromatic ring of the chromophore, where the negative charge is delocalized. No other positively charged side chains neighbor the chromophore. The phenolic oxygen of the chromophore hydrogen bonds with Tyr42 $O_\eta$ and Glu46 $O_{\epsilon 1}$ (in an *anti* configuration, Figure 5A). An integral part of the active site, Glu46 is completely buried inside the protein and presumably in a protonated (uncharged) state, with its carboxylic proton shared with the phenolic oxygen of the chromophore. Thr50 has a central role: not only does its side-chain $O_{\gamma 1}$ atom hydrogen bond with Tyr42 $O_\eta$ and with the carbonyl oxygen of Glu46 but its main-chain carbonyl oxygen also hydrogen bonds with Arg52 (Figure 5A). These four side chains are contributed by helix α3 and flanking residues in the short, adjacent, connecting loops (see Figures 2C, 3, and 5A). Together, these interactions with the protein maintain the chromophore's negative charge and resultant yellow color in the dark state.

Arg52 is held between the chromophore and solvent by hydrogen bonds with the carbonyl oxygen atoms of Thr50 and Tyr98 (Figure 5A). This structural arrangement implicates Arg52 in two important roles. First, the close proximity of the positively charged guanidinium group (Arg52 $N_\epsilon$ is 3.7 Å away from the chromophore ring) helps stabilize and delocalize the buried negative charge on the chromophore. Second, Arg52 shields the chromophore from solvent and is the most likely gateway for the phototactic signal (captured by the chromophore) to be transmitted to the outside of the protein.

*Electrostatic Asymmetry on the Protein Surface*. The molecular surface of PYP exhibits a striking electrostatic feature adjacent to active site Arg52 (Figure 5B): a large (687 Å$^2$; 13% of the total surface) patch of negative electrostatic potential (−13 to −4 kcal/mol), formed predominantly by helices α1, α2, and α3. Four of the six acidic side chains contributing to the negative electrostatic potential come from the N-terminal helical lariat and two from the helices flanking Arg52. The surface patch immediately surrounding Arg52 is concave with weakly positive electrostatic potential (+2 to +4 kcal/mol). Interestingly, the adjacent dominant negative patch includes the binding site for the $Gd^{2+}$ ion (Table 2), which is a mimic of the $Ca^{2+}$ ion, a key player in vertebrate and invertebrate phototransduction (Hardie, 1993; Lagnado & Baylor, 1994). It is not known which second messengers (i.e., proteins, small molecules, or ions) interact with PYP. However, the large negative molecular surface patch, the cation binding site, and the active site Arg form an obvious, accessible, recognition face for molecules receiving the phototactic signal.

*Comparison with the Retinal-Containing Rhodopsin Family*. PYP and bR share common and complementary active site features related to their photocycles, despite their very different folds. Both active sites stabilize a buried, charged, highly conjugated, covalently bound chromophore with

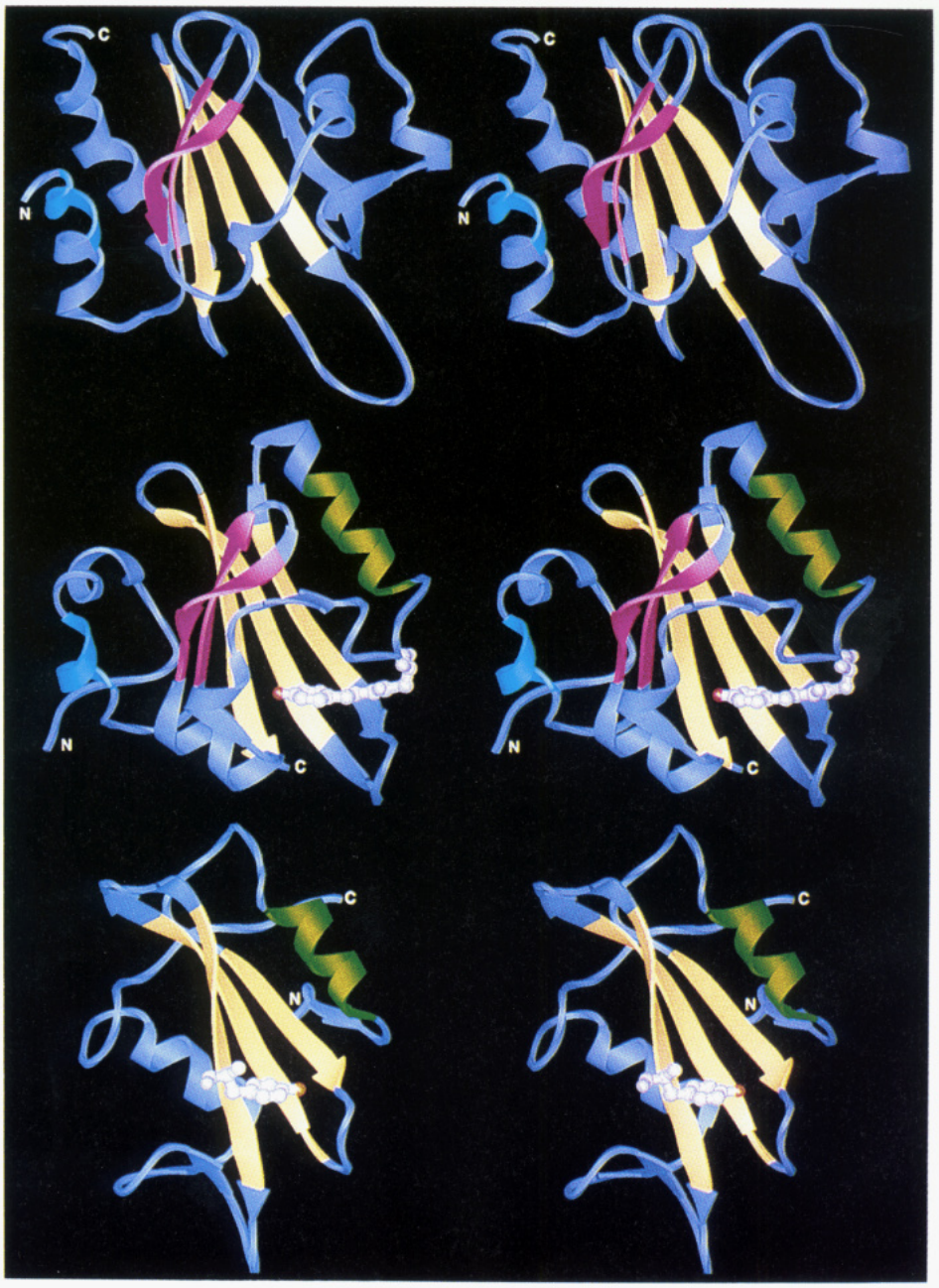


FIGURE 4: Structural and topological motifs in PYP (center) shared with profilin (top) and the SH2 domain (bottom) shown as stereo pairs. The twist and topology of the three common (yellow) $\beta$-strands are conserved in all three folds and not in any other structures examined. The two pink $\beta$-strands and a light blue helical turn are conserved between profilin and PYP. The green $\alpha$-helix is conserved between PYP and the SH2 domain. Nonconserved structural elements are shown in blue. For comparison with profilin (Schutt et al., 1993), 28 $C_\alpha$ atoms of five $\beta$-strands were superimposed (root mean square deviation 0.8 Å): PYP 30−34, 38−42, 89−93, 105−110, and 117−123 onto profilin 19−23, 29−33, 84−88, 98−103, and 108−114. For comparison with the SH2 domain of the v-*src* oncogene product with phosphotyrosyl peptide bound [Brookhaven Protein Data Bank entry 1SHA (Waksman et al., 1992)], 21 $C_\alpha$ atoms of three $\beta$-strands were superimposed (root mean square deviation 0.9 Å): PYP 89−93, 105−112, and 117−124 onto SH2 29−33, 40−47, and 55−62. For this figure, the three superimposed structures were offset vertically. Interestingly, the phenyl rings of the PYP chromophores and the phosphotyrosine (balls and sticks) bound to SH2 are only 2.1 Å apart after superposition of topologically equivalent $\beta$-strands.

complementary charged side chains and a hydrogen-bonding network. Both active sites are characterized by buried acidic side chains (Glu46 in PYP and Asp85, Asp96, and Asp212 in bR), a buried Thr (Thr50 in PYP and Thr46 in bR), and an Arg near the surface (Arg52 in PYP and Arg82 in bR). In the dark state, PYP's chromophore is anionic (Baca et al., 1994), whereas bR's chromophore is cationic (Krebs & Khorana, 1993). PYP exhibits a net uptake of one proton upon bleaching and a net release of one proton upon return to the dark state (Meyer et al., 1993). Conversely, the retinal Schiff base of bR is deprotonated upon bleaching and reprotonated upon recovery (Krebs & Khorana, 1993). Thus, the active site structures of both proteins mediate the coupled changes in color and protonation states that are characteristic of their light cycles.

In the photocycles of the retinal-containing rhodopsin family, the energy from light is converted into atomic motion by *trans*−*cis* isomerization of the chromophore (Wald, 1968). The atomic structure of PYP has implications for this expected chromophore isomerization and the resulting signal transduction steps. In PYP, close contacts between the thioester carbonyl oxygen and the aromatic ring would strain a *cis* conformation of the 4-hydroxycinnamyl chromophore, precluding a fully planar *cis* conformer and predicting a short

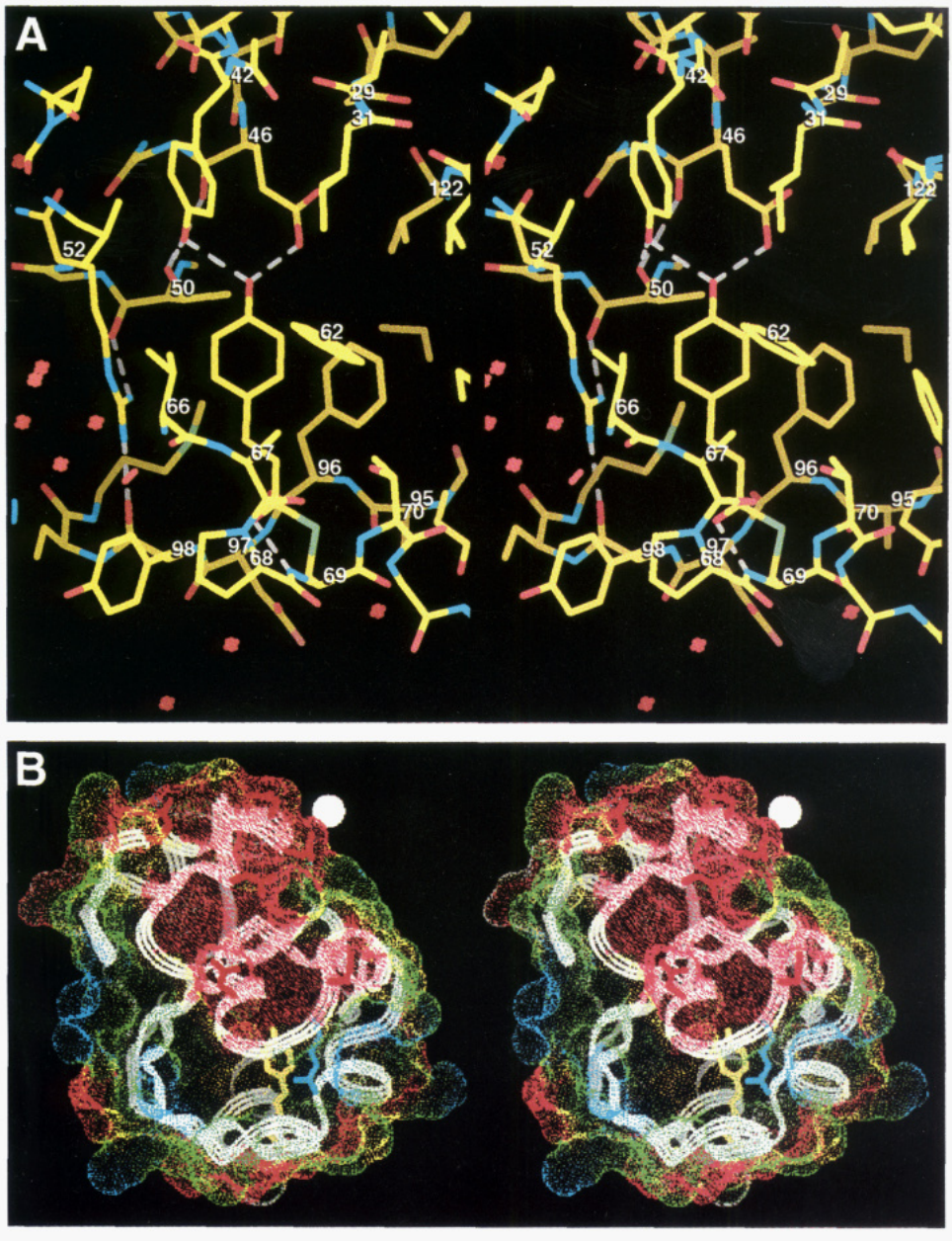


FIGURE 5: Stereoview of the PYP active site and structurally implicated recognition surface. (A) PYP active site, showing the 4-hydroxycinnamyl chromophore (center) bound to Cys69 via a thioester linkage (bottom). The model is colored as in Figure 1A. The hydrophobic core is to the right, and the solvent (water molecules shown as red crosses) is to the left of Arg52. The terminal, phenolic oxygen of the chromophore hydrogen bonds (dashed gray lines) with Tyr42 $O_\eta$ and Glu46 $O_{\epsilon 1}$ and packs against Thr50 $C_{\gamma 2}$. Five residues from the major hydrophobic core (Ile31 from $\beta$1, Phe62 from $\beta$3, Val66 and Ala67 from the chromophore loop, and Phe96 from $\beta$4) pack against the ring of the chromophore. The chromophore-containing tight turn (Ala67, Pro68, Cys69, and Thr70) covers the thioester linkage. The thioester carbonyl oxygen forms a hydrogen bond with its own main-chain N. The main-chain atoms of Thr95, Asp97, and Tyr98 (from $\beta$4 and the following loop) complete the protein contacts within 4 Å of the chromophore. Thr50 $O_{\gamma 1}$ hydrogen bonds with Tyr42 $O_\eta$ and with the carbonyl oxygen of Glu46, and Arg52 hydrogen bonds with the carbonyl oxygen atoms of Thr50 and Tyr98. Besides the hydrogen bond with the chromophore, Glu46 makes hydrophobic contacts with Gly29 $C_\alpha$ (3.3 Å), Ile31 $C_\delta$ (3.7 Å), Thr50 $C_{\gamma 2}$ (3.5 Å), and Val122 $C_{\gamma 2}$ (3.7 Å). (B) Structurally implicated recognition surface of PYP, shown with a ribbon trace and critical side chains. The PYP molecular surface, shown as dots colored by electrostatic potential (red, negative; yellow/green, neutral; and blue, positive; see Methods), reveals a unique, large (687 Å$^2$), negatively charged surface patch (red dots) that dominates the electrostatic surface and is located above the active site. In this view, the molecule is oriented with the central $\beta$-sheet on edge with $\beta$-strands 45° to the horizontal (from lower left to upper right) and with $\beta$3 forward (white ribbon indicates the fold). The N-terminal helical lariat is at the top, and the loop containing the chromophore (yellow bonds) is at the bottom. The probable recognition face for signal transduction includes the $Gd^{2+}$ binding site (white sphere, upper right), the six acidic residues (Glu2, Asp19, Asp20, Asp24, Asp48, and Asp53; red bonds) of the negative patch, and Arg52 (blue bonds, lower right). There are also three minor (3−4% of the total surface) negative patches (electrostatic potential between −13 and −4 kcal/mol) on the surface of PYP (not shown): a 172 Å$^2$ patch (back face), a 244 Å$^2$ patch (right face), and a 220 Å$^2$ patch (bottom face). Positive electrostatic potential (+4 to +9 kcal/mol; blue dots) accounts for <2% of the total PYP surface.

lifetime for this intermediate. Additionally, a *cis* conformer would collide within the tightly packed PYP active site, causing motion of the surrounding residues and thereby transmitting the phototactic signal.

*Significance.* The 1.4 Å structure of PYP reported here provides definitive atomic information on a protein photosensor. This structure will contribute to a variety of computational and experimental studies aimed at establishing

the atomic basis for a protein's photocycle. The surprising similarities of the PYP fold, a motif previously unrecognized in prokaryotes, to portions of eukaryotic SH2 and profilin domains demonstrate unexpected common features among signal transduction proteins and pathways. Thus, this PYP structure provides the basis for achieving both a more detailed and unified understanding of these key biological signals and receptors.

## ACKNOWLEDGMENT

We thank Susan L. Bernstein, Jessica Bessler, Darren J. Murtari, Nikhil Munshi, and Kelly A. Slater for technical assistance; John A. Tainer, Duncan E. McRee, Susan M. Redford, Brian R. Crane, Thomas Terwilliger, C. David Stout, and Hans E. Parge for valuable discussions; Terry E. Meyer for *E. halophila* strain BN9626; Michael E. Pique for help with graphics and the electron density gradient calculation; Cindy L. Fisher for help with atom partial charge assignment; Manuel Baca for discussions on proposed chromophore mechanisms; Patrick M. Burke for growing the large crystal used for the 1.4 Å resolution native diffraction data set; and Clarence E. Schutt and Michael D. Rozycki for the profilin coordinates.

## REFERENCES

Alexandrov, N. N., & Gō, N. (1994) *Protein Sci. 3*, 866−875.
Baca, M., Borgstahl, G. E. O., Boissinot, M., Burke, P. M., Williams, D. R., Slater, K. A., & Getzoff, E. D. (1994) *Biochemistry 33*, 14369−14377.
Birge, R. R. (1990) *Annu. Rev. Phys. Chem. 41*, 683−733.
Bogomolni, R. A., & Spudich, J. L. (1982) *Proc. Natl. Acad. Sci. U.S.A. 79*, 6250−6254.
Brünger, A. T. (1992) *Nature 355*, 472−474.
Brünger, A. T. (1993) *Acta Crystallogr., Sect. D 49*, 24−36.
Brünger, A. T., & Nilges, M. (1993) *Q. Rev. Biophys. 26*, 49−125.
Brünger, A. T., Kuriyan, J., & Karplus, M. (1987) *Science 235*, 458−460.
Brünger, A. T., Krukowski, A., & Erickson, J. W. (1990) *Acta Crystallogr., Sect. A 46*, 585−593.
Carson, M. (1991) *J. Appl. Crystallogr. 24*, 958−961.
Connolly, M. L. (1983) *J. Appl. Crystallogr. 16*, 548−558.
Hardie, R. C. (1993) *Nature 366*, 113−114.
Henderson, R., Baldwin, J. M., Ceska, T. A., Zemlin, F., Beckmann, E., & Downing, K. H. (1990) *J. Mol. Biol. 213*, 899−929.
Hoff, W. D., Düx, P., Hård, K., Devreese, B., Nugteren-Roodzant, I. M., Crielaard, W., Boelens, R., Kaptein, R., Van Beeumen, J., & Hellingwerf, K. J. (1994a) *Biochemistry 33*, 13960−13962.
Hoff, W. D., Sprenger, W. W., Postma, P. W., Meyer, T. E., Veenhuis, M., Leguijt, T., & Hellingwerf, K. J. (1994b) *J. Bacteriol. 176*, 3920−3927.
Holm, L., & Sander, C. (1990) *J. Mol. Biol. 233*, 123−138.
Howard, A. J., Gilliland, G. L., Finzel, B. C., Poulos, T. L., Ohlendorf, D. H., & Salemme, F. R. (1987) *J. Appl. Crystallogr. 20*, 383−387.
Imhoff, J. F., Hashwa, F., & Trüper, H. G. (1978) *Arch. Hydrobiol. 84*, 381−388.
Jones, T. A., Zou, J. Y., Cowan, S. W., & Kjeldgaard (1991) *Acta Crystallogr., Sect. A 47*, 110−119.
Kabsch, W., & Sander, C. (1983) *Biopolymers 22*, 2577−2637.
Koch, C. A., Anderson, D., Moran, M. F., Ellis, C., & Pawson, T. (1991) *Science 252*, 668−674.
Krebs, M. P., & Khorana, H. G. (1993) *J. Bacteriol. 175*, 1555−1559.
Lagnado, L., & Baylor, D. A. (1994) *Nature 367*, 273−277.
Laskowski, R. A., MacArthur, M. W., Moss, D. S., & Thornton, J. M. (1993) *J. Appl. Crystallogr. 26*, 283−291.
Lassing, I., & Lindberg, U. (1985) *Nature 314*, 472−474.
Leslie, A. G. W., Brick, P., & Wonacott, A. J. (1986) *CCP4 News 18*, 33.
McRee, D. E. (1992) *J. Mol. Graphics 10*, 44−46.
McRee, D. E. (1993) *Practical Protein Crystallography*, Academic Press, Inc., San Diego, CA.
McRee, D. E., Meyer, T. E., Cusanovich, M. A., Parge, H. E., & Getzoff, E. D. (1986) *J. Biol. Chem. 261*, 13850−13851.
McRee, D. E., Tainer, J. A., Meyer, T. E., Van Beeumen, J., Cusanovich, M. A., & Getzoff, E. D. (1989) *Proc. Natl. Acad. Sci. U.S.A. 86*, 6533−6537.
Meyer, T. E. (1985) *Biochim. Biophys. Acta 806*, 175−183.
Meyer, T. E., Yakali, E., Cusanovich, M. A., & Tollin, G. (1987) *Biochemistry 26*, 418−423.
Meyer, T. E., Tollin, G., Hazzard, J. H., & Cusanovich, M. A. (1989) *Biophys. J. 56*, 559−564.
Meyer, T. E., Fitch, J. C., Bartsch, R. G., Tollin, G., & Cusanovich, M. A. (1990) *Biochim. Biophys. Acta 1016*, 364−370.
Meyer, T. E., Cusanovich, M. A., & Tollin, G. (1993) *Arch. Biochem. Biophys. 306*, 515−517.
Ng, K., Getzoff, E. D., & Moffat, K. (1995) *Biochemistry 34*, 879−890.
Purvis, G. D., & Culberson, C. (1986) *J. Mol. Graphics 4*, 88−92.
Ramachandran, G. N., & Sasisekharan, V. (1968) *Conformation of polypeptide and proteins*, Vol. 23, Academic Press, New York.
Roberts, V. A., Freeman, H. C., Olson, A. J., Tainer, J. A., & Getzoff, E. D. (1991) *J. Biol. Chem. 266*, 13431−13441.
Schertler, G. F. X., Villa, C., & Henderson, R. (1993) *Nature 362*, 770−772.
Schutt, C. E., Myslik, J. C., Rozycki, M. D., Goonesekere, N. C. W., & Lindberg, U. (1993) *Nature 365*, 810−816.
Sprenger, W. W., Hoff, W. D., Armitage, J. P., & Hellingwerf, K. J. (1993) *J. Bacteriol. 175*, 3096−3104.
Spudich, E. N., Takahashi, T., & Spudich, J. L. (1989) *Proc. Natl. Acad. Sci. U.S.A. 86*, 7746−7750.
Spudich, J. L., & Bogomolni, R. A. (1988) *Annu. Rev. Biophys. Biophys. Chem. 17*, 193−215.
Tilney, L. G., Bonder, E. M., Coluccio, L. M., & Mooseker, M. S. (1983) *J. Cell Biol. 97*, 112−124.
Upson, C., Faulhaber, T., Jr., Kamins, D., Laidlaw, D., Schlegel, D., Vroom, J., Gurwitz, R., & van Dam, A. (1989) *IEEE Comput. Graphics Appl. 9*, 30−42.
Waksman, G., Kominos, D., Robertson, S. C., Pant, N., Baltimore, D., Birge, R. B., Cowburn, D., Hanafusa, H., Mayer, B. J., Overduin, M., Resh, M. D., Rios, C. B., Silverman, L., & Kuriyan, J. (1992) *Nature 358*, 646−653.
Wald, G. (1968) *Nature 219*, 800−807.
Weiner, S. J., Kollman, P. A., Case, D. A., Singh, U. C., Ghio, C., Alagona, G., Profeta, S., Jr., & Weiner, P. (1984) *J. Am. Chem. Soc. 106*, 765−784.
Zhang, K. Y. J. (1993) *Acta Crystallogr., Sect. D 49*, 213−222.
Zhang, K. Y. J., & Main, P. (1990) *Acta Crystallogr., Sect. A 46*, 377−381.

BI9503256